J. Fluid Mech. (2016), *vol.* 808, *pp.* 511–538. © Cambridge University Press 2016
doi:10.1017/jfm.2016.665

Skin-friction generation by attached eddies in turbulent channel flow

Matteo de Giovanetti[1], Yongyun Hwang[1,†] and Haecheon Choi[2]

[1]Department of Aeronautics, Imperial College London, South Kensington SW7 2AZ, UK

[2]Department of Mechanical and Aerospace Engineering, Seoul National University, Seoul 08826, South Korea

(Received 10 March 2016; revised 4 October 2016; accepted 11 October 2016;
first published online 3 November 2016)

Despite a growing body of recent evidence on the hierarchical organization of the self-similar energy-containing motions in the form of Townsend's attached eddies in wall-bounded turbulent flows, their role in turbulent skin-friction generation is currently not well understood. In this paper, the contribution of each of these self-similar energy-containing motions to turbulent skin friction is explored up to $Re_\tau \simeq 4000$. Three different approaches are employed to quantify the skin-friction generation by the motions, the spanwise length scale of which is smaller than a given cutoff wavelength: (i) FIK (Fukagata, Iwamoto, Kasagi) identity in combination with the spanwise wavenumber spectra of the Reynolds shear stress; (ii) confinement of the spanwise computational domain; (iii) artificial damping of the motions to be examined. The near-wall motions are found to continuously reduce their role in skin-friction generation on increasing the Reynolds number, consistent with the previous finding at low Reynolds numbers. The largest structures given in the form of very-large-scale and large-scale motions are also found to be of limited importance: due to a non-trivial scale interaction process, their complete removal yields only a 5–8 % skin-friction reduction at all of the Reynolds numbers considered, although they are found to be responsible for 20–30 % of total skin friction at $Re_\tau \simeq 2000$. Application of all the three approaches consistently reveals that the largest amount of skin friction is generated by the self-similar motions populating the logarithmic region. It is further shown that the contribution of these motions to turbulent skin friction gradually increases with the Reynolds number, and that these coherent structures are eventually responsible for most of turbulent skin-friction generation at sufficiently high Reynolds numbers.

Key words: turbulence simulation, turbulence theory, turbulent boundary layers

1. Introduction

The reduction of skin friction in wall-bounded turbulent shear flows is an important goal to decrease energy expenditure in many industrial sectors. It has a wide range of engineering applications ranging from massive pipelines for oil and gas transport to almost all types of vehicles, ground, air or sea based. Many of these applications typically take place at high Reynolds numbers, and a wealth of systems and techniques to reduce turbulent skin-friction drag have been proposed over many years. In

† Email address for correspondence: y.hwang@imperial.ac.uk

practice, only very few of these systems and techniques have been implemented with any success, and many of them appear to be subject to a performance loss as the Reynolds number increases, as well as suffering from other technical constraints (Bushnell 2002; García-mayoral & Jiménez 2011; Quadrio 2011; Kornilov 2015). At low Reynolds numbers, the origin of turbulent skin friction has been inextricably linked to the near-wall region. In this region, the interaction between two predominant coherent structures, streaks (Kline *et al.* 1967) and quasi-streamwise vortices (Kim, Moin & Moser 1987; Jeong & Hussain 1997), with a mean spanwise spacing of $\lambda_z^+ \approx 100$, plays a central role in turbulent production (Jiménez & Moin 1991; Hamilton, Kim & Waleffe 1995; Schoppa & Hussain 2002). The interactive process is essentially independent of the motions in the logarithmic and outer regions, as it survives even when the motions in the logarithmic and outer regions are either poorly resolved (Jiménez & Moin 1991) or artificially damped out (Jiménez & Pinelli 1999; Hwang 2013). The generation of turbulent skin friction (or wall shear stress) has been understood to be directly linked to this near-wall process, and, in particular, the streamwise vortices have been found to be strongly correlated to the near-wall turbulent skin friction (Kravchenko, Choi & Moin 1993; Choi, Moin & Kim 1994; Orlandi & Jimenez 1994). This observation led to the design of flow control strategies aimed at direct disruption of the near-wall streamwise vortices: for example, spanwise oscillations (Stadsted & Moin 1991; Jung, Mangiavacchi & Akhavan 1992) and opposition control (Choi *et al.* 1994). All these control strategies perform very well at low Reynolds numbers with a considerable amount of turbulent drag reduction. However, it has recently been reported that their effectiveness deteriorates with increasing Reynolds number (Chang, Collis & Ramakrishnan 2002; Gatti & Quadrio 2013), even though the direct effect of these controls on the near-wall region appears to remain unchanged (Agostini, Touber & Leschziner 2014).

Over the past decade, there has been a substantial amount of evidence that the logarithmic and outer regions of wall-bounded turbulence are organised with remarkable coherence. The most well-known coherent structures in these regions are probably large-scale motions (LSMs) (Kovasznay 1970) and very-large-scale motions (VLSMs) (Kim & Adrian 1999; del Alamo & Jiménez 2003; Hutchins & Marusic 2007*a*). In particular, the latter structures were found to prevail over the entire wall-normal location (del Alamo *et al.* 2004; Tomkins & Adrian 2005), strongly influencing the near-wall region through direct penetration (del Alamo & Jiménez 2003; Hutchins & Marusic 2007*b*) and/or modulation of the near-wall processes (Mathis, Hutchins & Marusic 2009; Marusic, Mathis & Hutchins 2010; Agostini & Leschziner 2016). Wall shear stress was also reported to be affected by these large-scale structures (Abe, Kawamura & Choi 2004; Schlatter *et al.* 2009). Recently, Hwang (2013) showed that removal of the structures, the spanwise sizes of which are larger than $\lambda_z^+ \simeq 100$, leads to a substantial amount of reduction of skin-friction drag in turbulent channel flow. Importantly, the contribution of the isolated near-wall structures to wall shear stress was found to rapidly decay on increasing the Reynolds number, suggesting that a significant amount of turbulent skin friction originates from the logarithmic and outer regions. The large contribution of the structures above the near-wall region was also confirmed in a turbulent boundary layer more recently by Deck *et al.* (2014), who calculated contribution of large-scale outer structures to turbulent skin friction. In this work, the FIK identity (Fukagata, Iwamoto & Kasagi 2002), which calculates turbulent skin friction with the wall-normal distribution of the Reynolds shear stress, was used with the spectral contribution of the large-scale outer structures to the Reynolds shear stress.

Despite this important progress, it has only been in very recent years that the general organisation of coherent structures above the near-wall region has begun to be unveiled. A growing body of novel evidence has suggested that the logarithmic and outer regions are likely to be composed of statistically self-similar coherent structures, as originally hypothesized by Townsend (1961, 1976) and Perry & Chong (1982) who called each of these structures the 'attached eddy'. For example, recent numerical and laboratory experiments have confirmed the existence of the logarithmic wall-normal dependence of the streamwise and spanwise turbulence intensities (Jiménez & Hoyas 2008; Marusic *et al.* 2013; Lee & Moser 2015), as originally predicted by Townsend (1976). Very recently, Hwang (2015) directly computed the statistical structure of each of the hypothetical attached eddies using their self-sustaining nature (Hwang & Cossu 2010*b*, 2011). Based on the linearly growing feature of the spanwise length scale with the distance from the wall (Tomkins & Adrian 2003; del Alamo *et al.* 2004), he found that, in a turbulent channel, the energy-containing motions at each of the spanwise length scales between $\lambda_z^+ \simeq 100$ and $\lambda_z \simeq 1.5h$ (h is half height of the channel) are statistically self-similar to one another, demonstrating the existence of the hypothetical attached eddies. It was shown that the smallest attached eddies are characterized by $\lambda_z^+ \simeq 100$ and are composed of the well-known near-wall streaks and the quasi-streamwise vortices (see also Hwang 2013). On the other hand, the largest ones, characterized by $\lambda_z \simeq 1.5h$, consist of the VLSMs (outer streaks) and the LSMs (outer streamwise vortical structures) (for a detailed discussion, see Hwang 2015). The motions at the intermediate spanwise length scale between $\lambda_z^+ \simeq 100$ and $\lambda_z \simeq 1.5h$ were also given in the form of streaks and quasi-streamwise vortical structures, and their size is proportional to the distance from the wall. It was further shown that each of these attached eddies in the logarithmic and outer regions has the self-sustaining process almost identical to that in the near-wall region (Hamilton *et al.* 1995; Jiménez & Pinelli 1999; Schoppa & Hussain 2002): the self-sustaining process of each of the attached eddies is composed of streak amplification by streamwise vortical structures via the lift-up effect, breakdown of the amplified streak with secondary instability or transient growth and the following nonlinear regeneration of the streamwise vortical structures (see Bengana & Hwang 2015; Hwang & Bengana 2016).

Given the remarkable self-similarities of the energy-containing motions existing from the near-wall to the outer region (i.e. attached eddies), it would not be unreasonable to hypothesize that all of these energy-containing motions in the logarithmic and outer regions would involve turbulent skin-friction generation to some extent as the near-wall motions do. Townsend (1976) originally speculated on the possible influence of the attached eddies on skin-friction fluctuation through their 'inactive' component. The numerical experiments of Hwang (2013) at low Reynolds numbers (up to $Re_\tau \approx 660$ where Re_τ is the friction Reynolds number) also hinted that such an idea would be relevant, even to mean skin friction. Interestingly, very recent work by Renard & Deck (2016) revealed that the logarithmic region is mainly responsible for turbulent skin-friction generation by applying a theoretical formula based on the production of turbulent kinetic energy to an existing simulation database of a turbulent boundary layer.

The goal of the present study is to explore this issue from a structural viewpoint, by quantifying turbulent skin-friction generation using the self-similar coherent structures in the form of Townsend's attached eddies at moderately high Reynolds numbers (up to $Re_\tau \simeq 4000$). To this end, we introduce three different numerical simulation-based approaches, each of which independently quantifies the contribution of the energy-containing motions at each of the spanwise length scales to turbulent

skin friction: (i) the FIK-identity-based method with the spanwise wavenumber spectra from existing direct numerical simulation (DNS) data by modifying the approach of Deck *et al.* (2014); (ii) exclusion of the motions by confining the spanwise computational domain (Flores & Jiménez 2010; Hwang & Cossu 2011); (iii) artificial damping of the motions at certain spanwise length scales in a sufficiently large computational box through a body forcing. Particular emphasis of the present study is given to answering the questions of potential importance in the design of novel flow control strategies: what are the contributions of the largest attached eddies given by VLSMs and LSMs to turbulent skin-friction drag? Does their removal yield any appreciable skin-friction reduction? If so, is the amount of the drag reduction potentially interesting for flow control? How large is the contribution of the self-similar attached eddies in the logarithmic region? What is the role of the interaction between the attached eddies at different length scales in turbulent skin-friction generation?

This paper is organised as follows. In § 2, we introduce the three approaches quantifying turbulent skin-friction generation by the attached eddies at each spanwise length scale with validation of the numerical tools we use. The results of the three independent quantifications are given in § 3, and we will see that dominant turbulent skin-friction generation occurs in the logarithmic region where most of the self-similar energy-containing motions reside. A detailed discussion on the skin-friction generation by these motions is given in § 4 in relation to their self-sustaining process, scale interaction and flow control. This paper concludes with some remarks in § 5.

2. Numerical experiment

2.1. *Numerical methods*

The numerical experiments in the present study are performed with near-wall-resolved large-eddy simulations in a turbulent channel with half-height h. The streamwise, wall-normal and spanwise directions are denoted by x, y and z, respectively, and the corresponding velocities are denoted by u, v and w. A numerical solver, which has been previously validated with DNS (Hwang 2013) and large-eddy simulations (LES) (Hwang & Cossu 2010*b*, 2011), is used in the present study. In this solver, the streamwise and spanwise directions are discretized using Fourier series with 2/3 dealiasing rule, whereas the wall-normal direction is discretised using a second-order central difference. The time steps are semi-implicitly advanced with a fractional step method: a Crank–Nicholson method is used for terms with wall-normal derivatives, and a third-order Runge–Kutta method is used for all the remaining terms. Constant mass flux is imposed across the channel.

The residual stress of the present LES is approximated with an eddy viscosity based on the model proposed by Vreman (2004). The Vreman model was developed to closely match the theoretically predicted algebraic properties of subgrid-scale dissipation for an extensive database of flows. An important feature of this model is that dissipation by the eddy viscosity becomes relatively small in transitional and near-wall regions, not requiring any special treatment for the near-wall region. The model shows performance comparable to the standard dynamic Smagorinsky model (e.g. Germano *et al.* 1991), and its dynamic variant has recently demonstrated a range of applicability to several canonical flows (Park *et al.* 2006). For further details, the reader may refer to Vreman (2004) and Park *et al.* (2006).

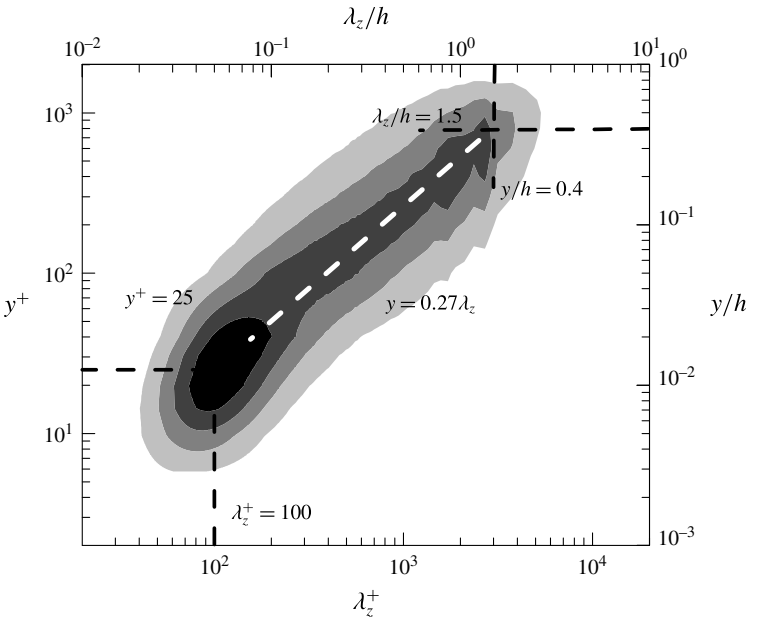

FIGURE 1. Premultiplied spanwise wavenumber spectra of the Reynolds shear stress at $Re_\tau = 2003$ in a turbulent channel flow (Hoyas & Jiménez 2006). The contour labels indicate 0.2, 0.4, 0.6, and 0.8 of the maximum, respectively.

2.2. *Assessment of skin-friction generation by self-similar attached eddies*

2.2.1. *FIK identity with spanwise wavenumber spectra*

The first approach is designed to follow the one recently proposed by Deck *et al.* (2014) who combined the streamwise wavenumber spectra of the Reynolds shear stress with the FIK identity (Fukagata *et al.* 2002) to calculate the contribution of large-scale outer structures to turbulent skin friction. In the present study, we use the spanwise wavenumber spectra, unlike the approach of Deck *et al.* (2014), as they are more instructive than the streamwise ones to identify the length scale of the energy-containing motions (Hwang 2015). Figure 1 shows the spanwise wavenumber spectra of the Reynolds shear stress in a turbulent channel flow at $Re_\tau = 2003$ (Hoyas & Jiménez 2006). The spectra are well aligned along the ridge given by $y \simeq 0.27\lambda_z$, indicating the linear spanwise scale growth with the distance from the wall. This feature enables us to clearly identify three different length scales of the energy-containing motions in wall-bounded shear flows: the inner ($\lambda_z^+ \simeq 100$), log-layer ($\lambda_z \sim y$) and outer ($\lambda_z \simeq 1.5h$) length scales. The motions at $\lambda_z^+ \simeq 100$ are composed of the near-wall streaks and the quasi-streamwise vortices (Hwang 2013), whereas the motions at $\lambda_z \simeq 1.5h$ are represented by the VLSMs (outer streaky structures) and the LSMs (outer streamwise vortical structures) (Hwang & Cossu 2010*b*; Hwang 2015). At the intermediate length scale between $\lambda_z^+ \simeq 100$ and $\lambda_z \simeq 1.5h$, the motions at each λ_z also consist of streamwise vortical structures and streaks, and they are self-similar to one another, forming the behaviour hypothesized by Townsend (1976) (i.e. attached eddy hypothesis). For further details, the reader may refer to Hwang (2015).

For a statistically stationary turbulent channel flow, the FIK identity gives the following relation between the skin-friction coefficient and the Reynolds shear stress:

$$C_f = \frac{12}{Re_m} + 12 \int_0^h 2\left(1 - \frac{y}{h}\right)\left(-\frac{\overline{u'v'}}{4U_m^2}\right) \mathrm{d}y, \tag{2.1}$$

where U_m is the bulk velocity. Here, the first term represents the contribution of the laminar part and the second term gives the contribution from turbulence. Using one-dimensional spanwise power spectral density $\Phi_{uv}(y; k_z)$, the Reynolds shear stress is written as

$$-\overline{u'v'}(y) = 2\int_0^\infty \Phi_{uv}(y; k_z)\,\mathrm{d}k_z, \tag{2.2}$$

where $k_z(= 2\pi/\lambda_z)$ is the spanwise wavenumber and the overbar denotes average in time and two homogenous directions. Here, the factor 2 in (2.2) is given to take the contribution of $\Phi_{uv}(y; k_z)$ for $k_z < 0$ into account. Equation (2.2) then enables us to calculate the Reynolds shear stress contribution of the motions, the spanwise size λ_z of which is smaller than a given cutoff wavelength $\lambda_{z,t}$, such that:

$$-(\overline{u'v'})_t(y; \lambda_{z,t}) = 2\int_{2\pi/\lambda_{z,t}}^\infty \Phi_{uv}(y; k_z)\,\mathrm{d}k_z, \tag{2.3}$$

where $(\overline{u'v'})_t$ is the Reynolds shear stress obtained with the spanwise wavenumber spectra for $\lambda_z < \lambda_{z,t}$. Substituting $(\overline{u'v'})_t$ into $\overline{u'v'}$ in (2.1) then leads to

$$C_{f,t}(\lambda_{z,t}) = \frac{12}{Re_m} + 12 \int_0^h 2\left(1 - \frac{y}{h}\right)\left(-\frac{(\overline{u'v'})_t(y; \lambda_{z,t})}{4U_m^2}\right) \mathrm{d}y, \tag{2.4}$$

yielding the skin-friction coefficient generated by the motions at $\lambda_z \leqslant \lambda_{z,t}$ and the laminar flow component: if $\lambda_{z,t} \to 0$, (2.4) yields the skin-friction coefficient given by the corresponding laminar flow. This approach is designed to apply to the existing data obtained by a full-scale simulation (DNS by Hoyas & Jiménez 2006), and quantifies the skin-friction generation by the motions at $\lambda_z \leqslant \lambda_{z,t}$ in the 'presence of all the motions'. It is also worth being noted that the last term on the right-hand side of (2.4), the key part of this approach, basically evaluates the amount of Reynolds shear stress at $\lambda_z \leqslant \lambda_{z,t}$ with a weight $1 - y/h$. This weight, which decreases linearly with y, gives more importance to the Reynolds shear stress carried by smaller structures in the region closer to the wall, and less importance to that of larger structures located further from the wall. Finally, it should be mentioned that this approach is solely based on a post processing of the computed data (i.e. the spanwise wavenumber spectra of Reynolds shear stress). Therefore, the approach does not affect other flow parameters and statistical quantities. We shall refer to this method as the 'FIK-identity-based approach'.

2.2.2. *Confining computational domain*

The second approach is based on the minimal box technique proposed by Hwang & Cossu (2010*b*, 2011) and Flores & Jiménez (2010) for the structures in the logarithmic and outer regions. The key parameter of this approach is the spanwise size of the computational domain L_z, as setting

$$L_z = \lambda_{z,t}, \tag{2.5}$$

allows one to simulate only the motions at $\lambda_z \leqslant \lambda_{z,t}$. This approach clearly differs from the FIK-identity-based approach as it quantifies skin-friction generation by the motions at $\lambda_z \leqslant \lambda_{z,t}$ in the absence of those at $\lambda_z > \lambda_{z,t}$. This approach was used by Hwang (2013) for the near-wall motions, and revealed that the contribution of the near-wall motions to turbulent skin friction decays rapidly with the Reynolds number. In the present study, we further extend this approach by considering an order of magnitude higher Reynolds number (up to $Re_\tau \simeq 4000$). The spanwise computational domain is also varied up to the largest spanwise length scale of the motions, $L_z = 1.5h$ (i.e. the spanwise length scale of the LSM and the VLSM).

In this approach, the constraint imposed on the spanwise domain size (2.5) provides the upper limit for the maximum finite value of λ_z. Nonetheless, the computational domain retains some motions at $\lambda_z > \lambda_{z,t}$ in the form of the spanwise uniform eddy: i.e. the motions at $\lambda_z \to \infty$ ($k_z = 0$). The eddy corresponding to this wavelength could still influence the remaining structures of the flow. In order to assess the influence of this uniform mode, the filter used in Hwang (2013) is also introduced to remove the $k_z = 0$ component of the streamwise and wall-normal velocities. This approach modifies the right-hand side of the momentum equation at each Runge–Kutta substep, such that:

$$\left.\begin{aligned} \widehat{\mathrm{RHS}}_x(y, k_x \neq 0, k_z = 0) = 0, \\ \widehat{\mathrm{RHS}}_y(y, k_x \neq 0, k_z = 0) = 0, \end{aligned}\right\} \tag{2.6}$$

where $\hat{\cdot}$ denotes the Fourier coefficient in the x and z directions, k_x is the streamwise wavenumber and RHS_x and RHS_y are respectively the right-hand sides of the streamwise and wall-normal components of the discretised momentum equation. More details of this technique, along with a broader discussion on its effects at low Reynolds numbers, can be found in Hwang (2013, 2015). With this technique, we will show that the effect of the spanwise uniform mode on the skin friction is very limited (see § 3.1 and appendix B).

It should be noted that, in applying this approach, considering a very long streamwise domain has been found not to be very critical (see also appendices A and B). This appears to be because the long streaky structures in the logarithmic and outer regions are well resolved with the streamwise uniform Fourier component. Indeed, the mean-velocity profile and skin-friction coefficient at a given Reynolds number have been found to be well recovered even with $L_x = 3.0h$ and $L_z = 1.5h$, consistent with previous studies (Flores & Jiménez 2010; Hwang & Cossu 2011; Lozano-Durán & Jiménez 2014). A careful examination has further revealed that the change of the streamwise domain yields a variation of the skin-friction coefficient only within 2 % if $L_x > 2L_z$ (appendix A). This amount of deviation is small enough for the given scope of the present study, as the skin friction has been found to vary up to 85 % with the designed numerical experiment (e.g. figure 6). This feature also allows us to explore a relatively wide range of the parameter space of Re_m and $\lambda_{z,t}$ without very long streamwise domain sizes. All the computations with this approach are therefore carried out with $L_x = 2L_z$. We note that this aspect ratio is equivalent to the smallest box size allowing for the self-sustaining process of the motions at each spanwise length scale L_z (Hwang & Cossu 2010*b*, 2011), and also corresponds well to the size of the self-similar vortex clusters (del Alamo *et al.* 2006). Simulation parameters for the biggest computational domain at four different Reynolds numbers are summarized in table 1. This method shall be referred to as the 'box-confinement approach'.

Case	Re_m	Re_τ	L_x/h	L_z/h	$N_x \times N_y \times N_z$	Δx^+	Δz^+	Δy_1^+
$M950$	38 100	951	3.0	1.5	$96 \times 81 \times 64$	44.6	33.4	1.80
$M2000$	89 100	2070	3.0	1.5	$144 \times 129 \times 144$	64.7	32.3	1.45
$M3000$	137 500	3042	3.0	1.5	$180 \times 151 \times 180$	76.0	39.1	1.83
$M4000$	193 200	4026	3.0	1.5	$288 \times 169 \times 288$	62.9	31.5	1.60

TABLE 1. Simulation parameters of the largest computational domain for the box-confinement approach (before dealiasing).

2.2.3. *Artificial damping of the motions*

The last approach employed is to compute skin-friction drag after eliminating the structures at $\lambda_z > \lambda_{z,t}$ in a sufficiently large computational domain. In this case, the removal of the motions at $\lambda_z > \lambda_{z,t}$ is implemented by introducing an artificial damping in the form of a body forcing to the right-hand side of the Navier–Stokes equation, such that:

$$\frac{\partial \boldsymbol{u}}{\partial t} + (\boldsymbol{\nabla} \cdot \boldsymbol{u})\boldsymbol{u} = -\frac{1}{\rho}\boldsymbol{\nabla} p + \nu \nabla^2 \boldsymbol{u} + \boldsymbol{f}, \tag{2.7}$$

where $\boldsymbol{u} = (u, v, w)$, t is time, ρ the density of fluid, p the pressure, ν the kinematic viscosity and $\boldsymbol{f}$ the introduced body forcing, respectively. To damp the motions at $\lambda_z > \lambda_{z,t}$, $\boldsymbol{f}$ is set for its Fourier component to satisfy

$$\hat{\boldsymbol{f}}(y, t; \lambda_x, \lambda_z) = -\mu(\lambda_z)\hat{\boldsymbol{u}}(y, t; \lambda_x, \lambda_z), \tag{2.8a}$$

with

$$\mu(\lambda_z) = \begin{cases} 0 & \text{for } \lambda_z \leqslant \lambda_{z,t}, \\ \mu_0 & \text{for } \lambda_z > \lambda_{z,t}, \end{cases} \tag{2.8b}$$

where $\hat{\cdot}$ denotes the Fourier coefficient in the x and z directions and λ_x is the streamwise wavelength. We note that the damping is also applied to $\lambda_z < 0$, but is not applied to zero spanwise wavenumber ($k_z = 0$) to make direct comparison with the result of the box-confinement approach without (2.6). A set of small different values of μ_0, ranging from 5.3×10^{-4} to 4.2×10^{-3}, have been chosen to minimize the effect of damping to other scales. These values have also been examined to check the robustness of this approach to the choice of μ_0. The statistics and skin-friction drag are found not to be appreciably dependent on the value of μ_0 considered and $\mu_0 = 1.4 \times 10^{-3}$ is used throughout the present study. The simulation parameters for this numerical experiment are summarized in table 2. Two computational domains are considered: one is with a sufficiently long streamwise domain ($F2000$) and the other is the minimal one for the largest structures ($W2000$). Most of the computations are performed with $W2000$, and a few cases are also verified with $F2000$. We shall call this method 'artificial damping'.

It should finally be noted that the approach damping the spanwise Fourier components for $\lambda_z > \lambda_{z,t}$ has an important difference from the box-confinement approach described in § 2.2.2. The box-confinement approach basically excludes the motions at $\lambda_z > \lambda_{z,t}$ by not resolving them except through zero spanwise wavenumber (i.e. $k_z = 0$). This implies that the motions at $\lambda_z \leqslant \lambda_{z,t}$ in a confined computational

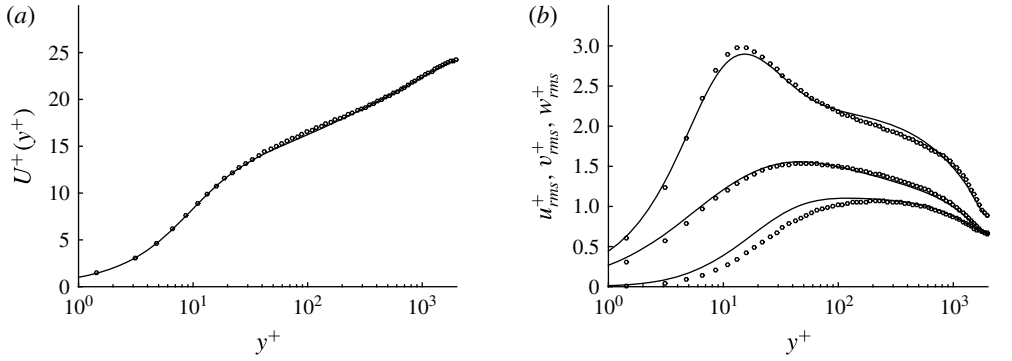

FIGURE 2. (*a*) Mean-velocity profile $U^+(y^+)$ and (*b*) turbulent velocity fluctuations at $Re_\tau \approx 2000$: ——, DNS by Bernardini, Pirozzoli & Orlandi (2014); ○, present LES (*F*2000).

Case	Re_m	Re_τ	L_x/h	L_z/h	$N_x \times N_y \times N_z$	Δx^+	Δz^+	Δy_1^+
*W*2000	89 100	2044	3.0	3.0	$144 \times 129 \times 288$	63.9	31.9	1.43
*F*2000	89 100	2056	12.0	3.0	$576 \times 129 \times 288$	64.3	32.1	1.44

TABLE 2. Parameters of reference simulation for artificial damping (before dealiasing).

domain have no way to transfer energy to the motions at $\lambda_z > \lambda_{z,t}$, except through zero spanwise wavenumber ($k_z = 0$). On the contrary, the damping approach allows for such energy transfer, and the transferred energy is damped in the range of the spanwise wavelengths at $\lambda_z > \lambda_{z,t}$. The two methods therefore do not necessary yield the same result.

2.3. *Validation*

The numerical experiment has been validated with several tests carried out at different values of Re_τ to appraise the performance of the Vreman model. Figure 2 compares the mean-velocity profile and turbulent velocity fluctuations of the present LES at $Re_\tau \simeq 2000$ (*F*2000) with those from DNS by Bernardini *et al.* (2014). Very good agreement is observed in the mean-velocity profile, and the velocity fluctuations also show acceptable agreement as well. The peak for the streamwise velocity fluctuation is slightly over-predicted, as it is commonly seen in LES. The spanwise and wall-normal components show somewhat smaller intensities than those of DNS, especially in the region closer to the wall, and this behaviour has been reported previously (Dukowicz & Dvinsky 1992; Kravchenko & Moin 1997; Sarghini, Piomelli & Balaras 1999; Gullbrand 2000).

In order to assess the suitability of the use of the box-confinement approach, the skin-friction coefficients with the largest computational domain in this case (i.e. $L_x = 3.0h$ and $L_z = 1.5h$) are compared with those obtained by experiment (Schultz & Flack 2013) and previous DNS (Hoyas & Jiménez 2006; Bernardini *et al.* 2014; Lozano-Durán & Jiménez 2014; Lee & Moser 2015) in figure 3. The present LES shows good agreement with both of the existing data and the empirical fit of Dean (1978) over the range of Re_m considered. The small difference at large Reynolds numbers ($Re_m > 10^5$)

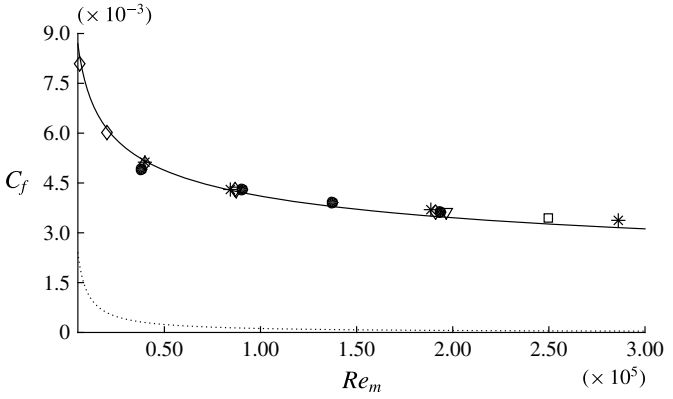

FIGURE 3. Variation of skin-friction coefficient with Re_m: ——, empirical fit of turbulent skin friction ($C_f = 0.073Re_m^{-0.25}$, Dean 1978); – – – –, laminar skin friction ($C_f = 12/Re_m$); ▽, DNS (Hoyas & Jiménez 2006; Lozano-Durán & Jiménez 2014); ◇, DNS (Bernardini *et al.* 2014); □, DNS (Lee & Moser 2015); ∗, experiment (Schultz & Flack 2013); ●, present LES ($L_x = 3.0h$ and $L_z = 1.5h$).

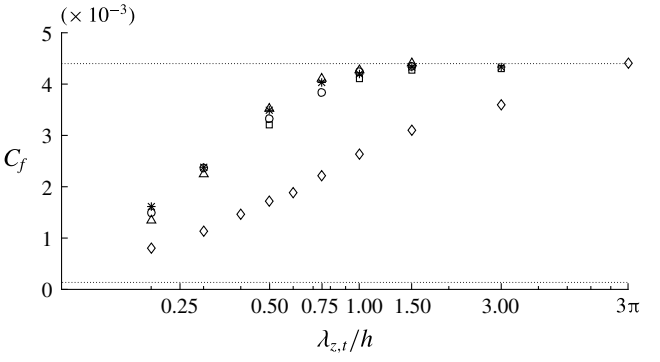

FIGURE 4. Variation of C_f with the cutoff spanwise wavelength $\lambda_{z,t}$ at $Re_\tau \simeq 2000$: ◇, FIK-identity-based approach; ∗, box-confinement approach (with spanwise uniform mode); △, box-confinement approach (without spanwise uniform mode) ○, artificial damping with $W2000$; □, artificial damping with $F2000$. Here, the upper and lower horizontal lines indicate turbulent (from DNS by Hoyas & Jiménez 2006) and laminar skin-friction coefficient ($C_f = 12/Re_m$), respectively.

appears to be due to a slight imprecision in Dean's original formula, and the issue has been recently addressed by Zanoun, Nagib & Durst (2009).

3. Results

3.1. *Skin-friction generation at* $Re_\tau \simeq 2000$

The skin-friction generation by the motions at $\lambda_z \leqslant \lambda_{z,t}$ is assessed by the three methods in § 2 at $Re_\tau \simeq 2000$ and is reported in figure 4. We note that the spanwise length of the largest energy-containing structures (VLSMs and LSMs) is $\lambda_z = 1.5h$, and that of the smallest ones (near-wall streaks and quasi-streamwise vortices) is $\lambda_z \simeq 0.05h$ (from $\lambda_z/h = \lambda_z^+/Re_\tau$ with $\lambda_z^+ = 100$) at this Reynolds number. The most immediate and evident conclusion in figure 4 is that, no matter which approach we

take, the spanwise scales in the range of $0.2h \leqslant \lambda_z \leqslant 1h$ are responsible for the largest portion of the skin friction and their removal leads to significant reduction of wall shear stress. The FIK-identity-based approach shows that this range of the spanwise scales is responsible for 41 % of total skin friction, while the box-confinement approach and the artificial damping reveal that around 60 % of skin-friction reduction is achieved by removing the motions at $\lambda_z > 0.2h$. This striking result implies that the largest amount of the skin friction at sufficiently high Reynolds numbers is generated by the self-similar energy-containing motions, most of which belong to the logarithmic region in the sense that their spanwise length scale is proportional to the distance from the wall.

An important difference is, however, observed between the skin frictions obtained with the FIK-identity-based approach and with the other two approaches. The FIK-identity-based method shows that the largest motions at $\lambda_z \geqslant 1.5h$ are responsible for a considerable amount of skin friction, i.e. 25–30 % of the total skin friction. This amount is not very far from that obtained by Deck *et al.* (2014), who computed the skin-friction generation by large-scale structures using the streamwise spectra for $\lambda_x >$ 1–2δ in a turbulent boundary layer (δ is the boundary-layer thickness). This approach also shows that skin-friction generation by the spanwise length scales of $\lambda_z > 1.5h$ is not negligible, despite the fact that the spanwise length of both the VLSMs and the LSMs is $\lambda_z \simeq 1.5h$. This is because the spanwise wavenumber spectra from the DNS with a large spanwise computational domain ($L_z = 3\pi$) contain a non-negligible amount of energy for $\lambda_z > 1.5h$ (see also figure 1). However, the box-confinement approach and the artificial damping, both of which show very similar behaviour to each other, yield very different trend of C_f with $\lambda_{z,t}$ from the FIK-based approach. In particular, both of the box-confinement approach and the artificial damping do not yield any significant change in C_f until the cutoff spanwise wavelength is reduced to $\lambda_{z,t} =$ 1–1.5h. A sensible amount of skin-friction reduction (4–8 %) is observed only when $\lambda_{z,t} \simeq 0.75$–$1.0h$, by which the largest structures at $\lambda_z \simeq 1.5h$ are removed. Both of the box-confinement approach and the artificial damping consistently show larger skin friction than that obtained with the FIK-identity-based approach, indicating that removal of relatively large motions does not yield reduction of the skin friction for which they are responsible. It is difficult to explain this feature if we exclude the role of scale interaction in the skin-friction generation process. A detailed discussion on this issue will be given in § 4.1.

Finally, it is worth mentioning that the uniform spanwise mode in the box-confinement approach is found to have little influence on the skin friction, as also shown in figure 4. Indeed, the removal of the spanwise uniform mode with (2.6) slightly reduces the skin friction only for relatively small $\lambda_{z,t}$ (= 0.2–0.3h) by the removal of the spanwise uniform mode ($\triangle$ in figure 4). This implies that the direct interaction between the spanwise uniform mode and the motions at $\lambda_z \leqslant \lambda_{z,t}$ ($= L_z$) is probably very minor. Further detailed evaluation of the differences between simulations with and without the uniform spanwise mode is presented in appendix B.

3.2. *Different Reynolds numbers*

Since the box-confinement approach and the artificial damping do not yield very different skin friction (see also discussion in § 4.1), the assessment of the skin-friction generation by the motions at $\lambda_z \leqslant \lambda_{z,t}$ is further explored only with the box-confinement approach up to $Re_\tau \simeq 4000$. Figure 5 shows the skin-friction

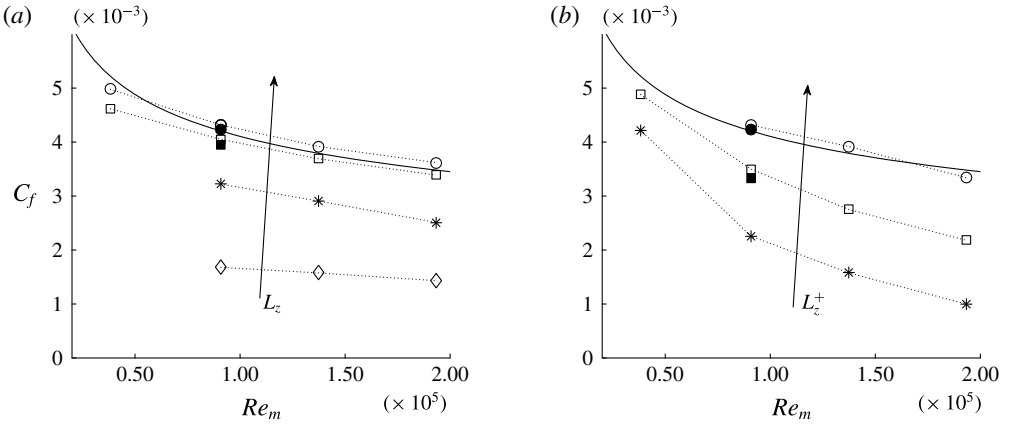

FIGURE 5. Variation of C_f with Re_m for the box-confinement approach (i.e. $L_z = \lambda_{z,t}$): (*a*) constant $L_z(= 0.2, 0.4, 0.75, 1.5h)$; (*b*) constant $L_z^+(\simeq 400, 1000, 3000)$. The filled square symbols (■) represent the artificial damping approach. Here, ——, C_f suggested by Dean (1978) ($C_f = 0.073Re_m^{-0.25}$).

generation with respect to $\lambda_{z,t}(=L_z)$ at four different Re_m. When L_z is chosen to scale with the outer unit, the reduced skin friction is found to follow a similar curvature with that of the full skin friction obtained with $L_z = 1.5h$ without any further deviation on increasing Re_m (figure 5*a*). In contrast, when L_z is set to scale with the inner unit, the deviation between C_f for $L_z^+ < 3000$ and that for $L_z^+ = 3000$ gradually increases with the Reynolds number. This implies that the contribution of the motions, the spanwise size of which is smaller than the given inner-scaled one, to total skin friction continuously decreases on increasing Re_m. This is consistent with the low Reynolds number result in Hwang (2013), who observed that the structures smaller than a fixed value of $L_z^+(\simeq 100,\ 200)$ yield decreasing portions of skin friction on increasing Re_m. The behaviour in figure 5 clearly suggests that, at very high Reynolds numbers, most of skin friction would be generated by the motions, the spanwise size of which lies between $\lambda_z^+ \approx 100$ and $\lambda_z \simeq 1.5h$. Given the size of these motions is proportional to the distance from the wall (i.e. $\lambda_z \sim y$), this indicates that the dominant skin-friction generation takes place essentially in the logarithmic region.

Finally, the reduced amount of skin friction by setting $L_z < 1.5h$ is found to approximately scale with the outer unit if the Reynolds number is sufficiently high. In figure 6, the skin-friction coefficients normalized by the reference one with $L_z = 1.5h$ are plotted with respect to L_z/h for all the Reynolds numbers considered. All the data, obtained at four different Re_m, appear to collapse approximately well into a single curve. For instance, a reduction in skin friction in the region of 7–8 % is obtained by halving the spanwise width (i.e. $L_z = 0.75h$). Another 10 % of the original friction is lost by reducing the box width to $L_z = 0.5h$. At $L_z = 0.2h$, the amount of skin friction generated is very close to 40 % of the initial value for all three of the larger Reynolds number.

3.3. *Probability density function of turbulent skin friction*

To further investigate how the statistical behaviour of turbulent skin-friction generation is changed by the removal of the structures at $\lambda_z > \lambda_{z,t}$, probability density functions

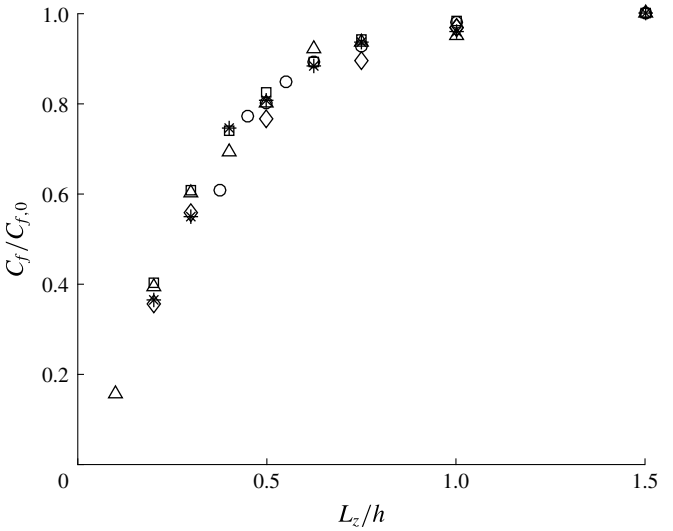

FIGURE 6. Variation of normalized skin-friction coefficient with $L_z(=\lambda_{z,t})$: ○, $Re_m =$ 38 100; ∗, $Re_m = 89\,100$; ◇, $Re_m = 89\,100$, artificial damping; □, $Re_m = 137\,500$; △, $Re_m =$ 193 200.

(PDFs) of skin friction are computed with the box-confinement approach ($\lambda_{z,t} = L_z$) at $Re_\tau \simeq 2000$. It has been found that the PDFs of instantaneous skin friction are positively skewed in a wide range of the Reynolds numbers (Keirsbulck, Labraga & Gad-El-Hak 2012; de Silva *et al.* 2014). This feature has often been interpreted to appear because the large-scale positive excursion of wall shear stress accompanies energetic small-scale wall shear stress fluctuations (Chernyshenko, Marusic & Mathis 2012; Mathis *et al.* 2013; Baars *et al.* 2015). The positive skewness of the PDFs also implies that if a high pass filter is applied to the instantaneous wall shear stress signal, its mean would be reduced, consistent with the observations in §§ 3.1 and 3.2.

Figure 7(*a*) shows the PDFs of the skin-friction coefficient C_f for several L_z. As L_z decreases, the peak location of the PDF moves towards smaller C_f, indicating reduction of mean skin friction. Also, the width of the PDFs is found to be decreased on decreasing L_z, suggesting that the variance of wall shear stress is also reduced by the decrease of L_z. Interestingly, the normalized PDFs, shown in figure 7(*b*), do not appear to be so different from one another, indicating that the skin-friction generation process in each confined computational domain is statistically self-similar. We note that, given the findings in §§ 3.1 and 3.2, the skin-friction generation process for all of the sufficiently large L_z would involve to some extent the hierarchical organization of self-similar energy-containing motions, the largest one of which is determined by the spanwise computational domain L_z. This implies that the only difference among the processes in different computational domains would stem from the largest energy-containing motions and the resulting extent of the hierarchical organization. Except for these, the processes in different computational domains are supposed to be similar to one another. This is clearly indicated by figure 7(*b*), also consistent with the notion that all the self-similar energy-containing motions throughout the entire wall-normal directions involve turbulent skin-friction generation.

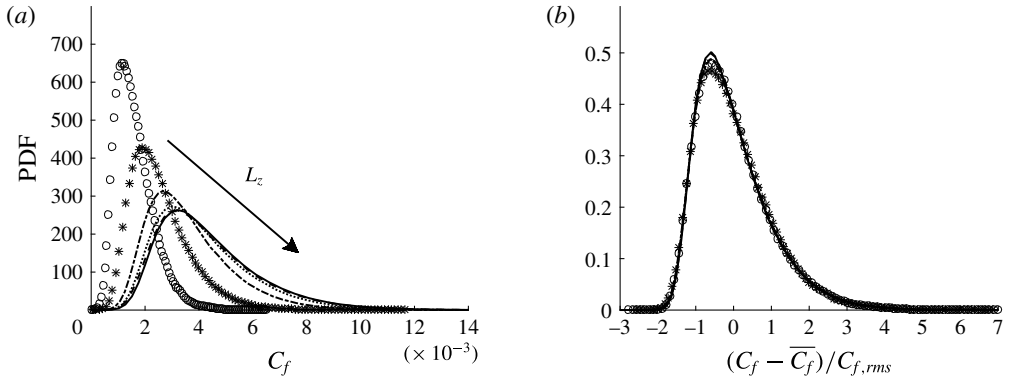

FIGURE 7. Probability density functions of instantaneous skin friction C_f from the box-confinement approach (i.e. $\lambda_{z,t} = L_z$) with (*a*) the original variable C_f and (*b*) normalized variable, $(C_f - \overline{C_f})/C_{f,rms}$ where $C_{f,rms}$ is the root mean square of C_f: ——, $L_z = 1.5h$; – – – –, $L_z = 1h$; · · · · · ·, $L_z = 0.75h$; – · – · –, $L_z = 0.5h$; ∗ $L_z = 0.3h$; ○ $L_z = 0.2h$.

4. Discussion

All the three independent approaches introduced in the present study consistently show that all the energy-containing motions ranging from the inner to the outer units are actively involved in turbulent skin-friction generation. In particular, the self-similar energy-containing motions at the spanwise length scale λ_z between $\lambda_z^+ \simeq 100$ and $\lambda_z \simeq 1.5h$ have been shown to be mainly responsible for turbulent skin-friction generation at sufficiently high Reynolds numbers. It is evident that the near-wall region gradually loses its dominant role in the friction generation on increasing the Reynolds number (figure 5*a*), consistent with previous findings (Chang *et al.* 2002; Gatti & Quadrio 2013; Hwang 2013). A little surprisingly, the contribution from the largest scales in the flow also appears to be limited. This is particularly true, as their removal does not result in reduction of the skin friction for which they are responsible (figure 4; see also a further discussion in § 4.3).

This finding is also consistent with the well-documented logarithmic growth of the near-wall streamwise turbulence intensity with the Reynolds number (Marusic & Kunkel 2003), i.e. the feature reflecting the increasing influence of the energy-containing motions in the logarithmic and outer regions to the near-wall region. The wall-attached part of each of the attached eddies is mainly composed of the streamwise and spanwise velocity components due to impermeability condition at the wall (Townsend 1976; Perry & Chong 1982; Hwang 2015). This therefore implies that the collective skin-friction generation by the self-similar energy-containing motions is probably a consequence of their near-wall influence, establishing a tight physical link with the logarithmic growth of the near-wall streamwise turbulence intensity with the Reynolds number. In this respect, it is also worth mentioning that this finding is consistent with very recent observation by Renard & Deck (2016), who identified the dominant contribution of the logarithmic region to skin-friction generation using a theoretical formula based on the mean streamwise kinetic-energy budget. Lastly, it is worth pointing out that DNS data for channel flow at $Re_\tau \approx 5200$ (Lee & Moser 2015) have shown an increase in the energy carried by the outer structures (the VLSM in particular) with a consequent impact on the velocity spectra as well. While this may potentially signify a more pronounced contribution of the largest scales to turbulent skin friction, it is difficult to disregard the observation made with figure 5(*b*) even at higher Reynolds numbers.

Finally, it should be pointed out that the wall-attached part of each of the attached eddies is 'inactive' in the sense that they carry very little Reynolds shear stress, since there is little wall-normal velocity in the vicinity to the wall (Townsend 1976; Hwang 2015). However, this does not necessarily imply that the inactive wall-attached part is not related to turbulent skin-friction generation, as the skin friction is nothing more than the streamwise velocity in the very vicinity to the wall, given its mathematical definition (i.e. $\nu\partial u/\partial y$ at the wall). This rather indicates that the energy-containing motions, which essentially reside in the logarithmic and outer regions, transport the streamwise momentum to the near-wall region through their inactive part, while generating Reynolds shear stress with their wall-detached wall-normal velocity component in the region much further from the wall. This transport process of the streamwise momentum by the wall-normal velocity described here is likely to be the so-called 'lift-up' effect (Cossu, Pujals & Depardon 2009; Hwang & Cossu 2010*a*), a part of the self-sustaining process extensively discussed in Hwang & Bengana (2016). The following discussion addresses this issue.

4.1. *Skin-friction generation and the self-sustaining process*

The concept of the self-sustaining process was originally proposed by Hamilton *et al.* (1995) for the near-wall motions, which were recently shown to be the smallest attached eddies (Hwang 2015; Hwang & Bengana 2016). The self-sustaining process is a cyclic dynamical process composed of three substeps: (i) the streaks are amplified by streamwise vortices via the lift-up effect, the process by which the streamwise vortices transfer the energy of the mean shear to the streaks (Landahl 1990; Kim & Lim 2000; Chernyshenko & Baig 2005; Cossu *et al.* 2009; Pujals *et al.* 2009; Hwang & Cossu 2010*a*); (ii) the amplified streaks break down with a sinuous-mode secondary instability and/or transient growth (Hamilton *et al.* 1995; Schoppa & Hussain 2002; Park, Hwang & Cossu 2011); (iii) the streamwise vortices are regenerated by nonlinear mechanisms (Hamilton *et al.* 1995; Schoppa & Hussain 2002; Hwang & Bengana 2016). It has recently been shown that the energy-containing motions in the logarithmic and outer regions bear the same self-sustaining process with a single turnover time period given by $Tu_\tau/\lambda_z \simeq 2$ (Hwang & Bengana 2016).

In the box-confinement approach, the size of the largest energy-containing motions is determined by the spanwise computational box size. The temporal evolution of these largest motions would therefore be reasonably well resolved by the flow quantities obtained by averaging over the computational domain, as also shown in Hwang & Bengana (2016). Using this approach, here we investigate the temporal evolution of each element in the self-sustaining process, and relate it with the generation of turbulent skin-friction drag by the largest scale in the given computational domain. For this purpose, we first introduce the following four integral quantities of interest:

$$E_u = \frac{1}{2L_xL_z}\int_0^{L_z}\int_0^{2/3L_z}\int_0^{L_x} u'^2\,\mathrm{d}x\,\mathrm{d}y\,\mathrm{d}z, \tag{4.1a}$$

$$E_v = \frac{1}{2L_xL_z}\int_0^{L_z}\int_0^{2/3L_z}\int_0^{L_x} v'^2\,\mathrm{d}x\,\mathrm{d}y\,\mathrm{d}z, \tag{4.1b}$$

$$E_1 = \int_0^{2/3L_z} |\hat{u}(y,k_x,k_z)|^2 + |\hat{v}(y,k_x,k_z)|^2 + |\hat{w}(y,k_x,k_z)|^2\,\mathrm{d}y, \tag{4.1c}$$

$$E_d = \frac{1}{L_xL_z}\int_0^{L_z}\int_0^{L_x} \tau_w\,\mathrm{d}x\,\mathrm{d}z, \tag{4.1d}$$

where $k_x = 2\pi/L_z$ and $k_z = 2\pi/L_z$ and τ_w is the instantaneous wall shear stress. Here, we note that the wall-normal domain for the integrations in (4.1) is defined to be $y \in [0,\ 2/3L_z]$ to include the most energetic part of the self-similar self-sustaining motions in each computational domain (see also Hwang & Bengana 2016, for further details). We also note that E_u represents the streaks, E_v the quasi-streamwise vortices and E_1 the streamwise meandering motions caused by streak instability, respectively, and their definitions exactly follow Hwang & Bengana (2016) where their physical relevance is extensively discussed. In the present study, we also introduce E_d, which would represent the instantaneous wall shear stress of the largest scale permitted by the given computational domain. However, one should bear in mind that E_d is not a full representation of the skin-friction generation by the largest structures in the domain, as it would not completely exclude the effect of smaller-scale structures on large-scale turbulent skin-friction generation.

To find exactly at which point in the self-sustaining process the skin-friction drag becomes maximized, we then compute temporal cross-correlation among these quantities in (4.1), such that:

$$C_{ij}(\tau) = \frac{\overline{E_i(t+\tau)E_j(t)}}{\sqrt{\overline{E_i^2}(t)}\sqrt{\overline{E_j^2}(t)}}, \tag{4.2}$$

with $i, j = u, v, 1, d$ from (4.1). Since an extensive discussion on the correlations among E_u, E_v and E_1 was given in Hwang & Bengana (2016), the focus in the present study will be mainly given to understanding of the cross-correlations involving the spatially averaged wall shear stress, i.e E_d.

The computed correlations, C_{ud}, C_{1d}, C_{vd} and C_{uv}, are shown in figure 8 for several different spanwise domains L_z. The cross-correlations with E_d reveal that at least their peak locations scale well with respect to the self-similar time scale $\tau u_\tau/L_z$. The correlations are also quite large: the peak values of C_{ud} and C_{vd} are greater than 0.6. In the cross-correlations, the peak location of C_{ud} is found to be at $\tau \approx -0.6$ (figure 8*a*), while those of C_{1d} and C_{vd} are at $\tau \approx -0.3 \sim -0.1$ (figure 8*b*,*c*). Unfortunately, it is difficult to find a clear difference between the peak locations of C_{1d} and C_{vd}. This is presumably because the streak instability, represented by E_1, is a fast dynamical process, as shown in Hwang & Bengana (2016). Further to this, it should be noted that all the flow quantities in (4.1) contain some effect of smaller-scale motions. In other words, these quantities do not precisely represent the structure of interest, yielding another complication. Nonetheless, the correlation C_{1v} in figure 8(*d*) clearly shows that the amplification of E_1 emerges before E_v reaches a large amplitude, consistent with Hwang & Bengana (2016). The cross-correlations in figure 8 therefore suggest that the sequence of the excursion of E_u (streak), E_1 (streak instability), E_v (streamwise vortical structure) and E_d (skin-friction generation) would be cyclically given as:

$$E_u \rightarrow E_1 \rightarrow E_v \rightarrow E_d. \tag{4.3}$$

The self-sustaining process is essentially a cyclic process represented by $E_u \rightarrow E_1 \rightarrow E_v$ with the single turnover time scale of $Tu_\tau/L_z \simeq 2$ (Hwang & Bengana 2016), and the process of $E_v \rightarrow E_u$ should follow with occurrence of the next cycle. Given the small time scale of the physical process of $E_v \rightarrow E_d$ at $\Delta\tau/L_z \approx 0.1$–$0.3$ (figure 8*c*), the only conclusion we can reach here would therefore be that the large amplification of E_d appears in the process of $E_v \rightarrow E_u$: i.e. the skin-friction generation by the

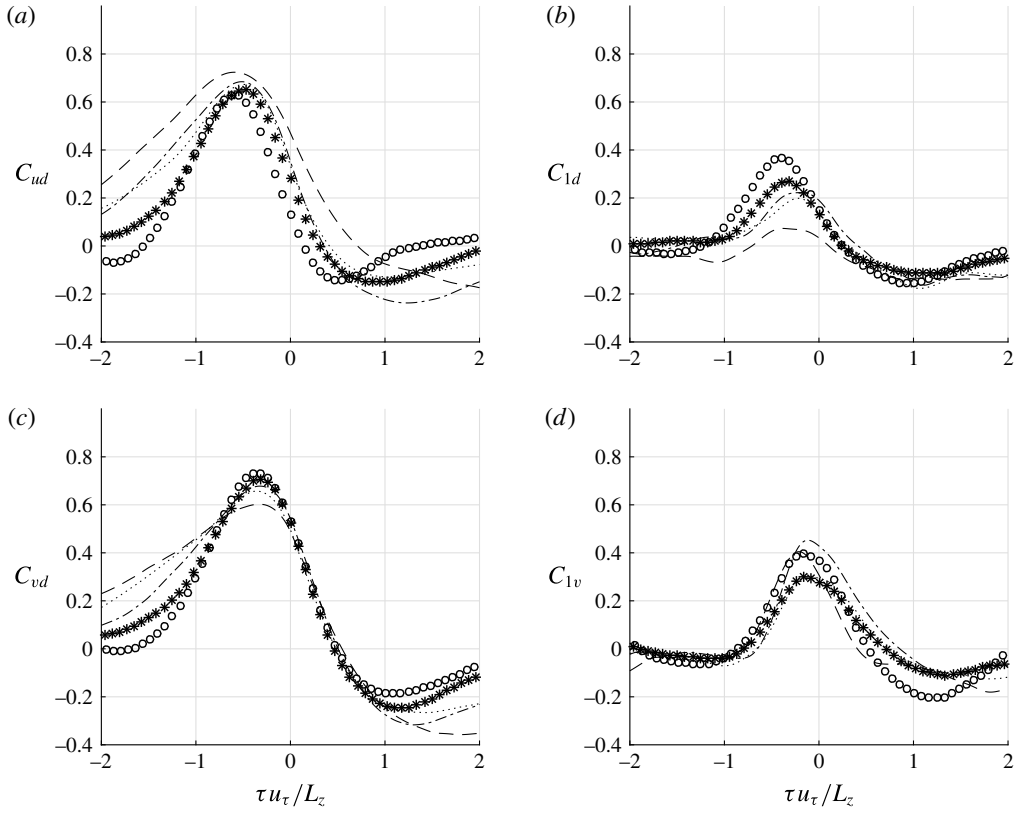

FIGURE 8. Cross-correlation functions obtained with the box-confinement approach ($\lambda_{z,t} = L_z$): (*a*) C_{ud}; (*b*) C_{1d}; (*c*) C_{vd}; (*d*) C_{1v}. Here, −−−−, $L_z = 1h$; ·····, $L_z = 0.75h$; −·−·−, $L_z = 0.5h$; ∗ $L_z = 0.3h$; ○ $L_z = 0.2h$.

largest structure (E_d) takes place when the streamwise vortices (E_v) are converted to the streak (E_u). This conversion of vortices to streaks is exactly the lift-up process, and the small time scale of the process of $E_v \rightarrow E_d$ suggests that the skin-friction generation is dominant at the early stage of the lift-up process. This observation is also consistent with the numerical experiment in Hwang & Bengana (2016) where the artificial suppression of the lift-up effect of the energy-containing motions in the logarithmic and outer regions was found to yield significant amounts of skin-friction reduction. Finally, it is important to highlight that the lift-up effect is a linear process, which is well described by the Navier–Stokes equation linearized around the mean flow (e.g. Cossu *et al.* 2009; Hwang & Cossu 2010*a*). Therefore, performing a linear analysis to understand skin-friction generation would provide a useful physical insight, as already demonstrated by a number of previous studies (e.g. Lim & Kim 2004; Moarref & Jovanović 2012; Blesbois *et al.* 2013; Luhar, Sharma & McKeon 2014).

4.2. *Scale interaction and skin-friction generation*

Although the three independent assessment methods in the present study consistently suggest that turbulent skin friction at sufficiently high Reynolds numbers is dominantly generated by self-similar motions in the logarithmic region, an important difference

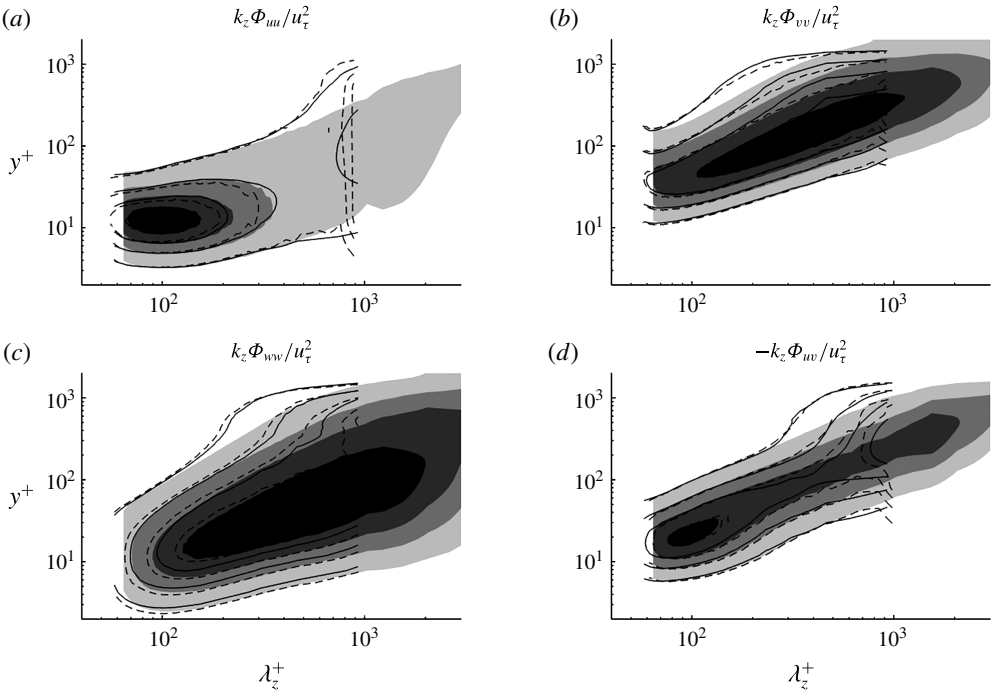

FIGURE 9. Premultiplied one-dimensional spanwise wavenumber spectra of (*a*) streamwise, (*b*) wall-normal, (*c*) spanwise velocities and (*d*) Reynolds shear stress. Here, the shaded, solid and dashed contours indicate the full domain simulation (*F*2000), the box-confinement approach and the artificial damping applied to *F*2000, respectively. For the box-confinement approach and the artificial damping, the cutoff spanwise wavelength is $\lambda_{z,t} = 0.5h$. The contour labels are chosen to be 0.2, 0.4, 0.6, 0.8 times each of the maximum for comparison.

between the FIK-identity-based approach and the other two approaches has also been observed (figure 4). This difference originates from the fact that the FIK-identity-based approach computes contribution of the motions at $\lambda_z \leqslant \lambda_{z,t}$ in the presence of all the structures, whereas the other two approaches actually remove the motions at $\lambda_z > \lambda_{z,t}$ during the simulation and calculate the skin friction with the remaining motions. It is evident that this large difference would not have been observed if there was no interaction among the energy-containing motions at different length scales.

To further understand the related scale interaction, one-dimensional spanwise wavenumber spectra from the LES with a sufficiently large spanwise domain (*F*2000), a confined box with $L_z = 0.5h$ and an artificial damping applied to *F*2000 with $\lambda_{z,t} = 0.5h$ are compared in figure 9. The spectra with the confined box and the artificial damping are quite different from those of the full simulation, particularly near $\lambda_z \simeq \lambda_{z,t}$. However, the two approaches, both of which physically remove the motions at $\lambda_z > \lambda_{z,t}$ from the simulations, do not yield very significant difference from each other in their spectra (see also figure 4). Overall, the spectral density of all the flow variables with the box-confinement approach and the artificial damping is found to be elevated compared to that of the full simulation particularly at the wall-normal location where the removed motions originally reside. Furthermore, this influence persists over a fairly wide range of the spanwise wavelength: the wall-normal

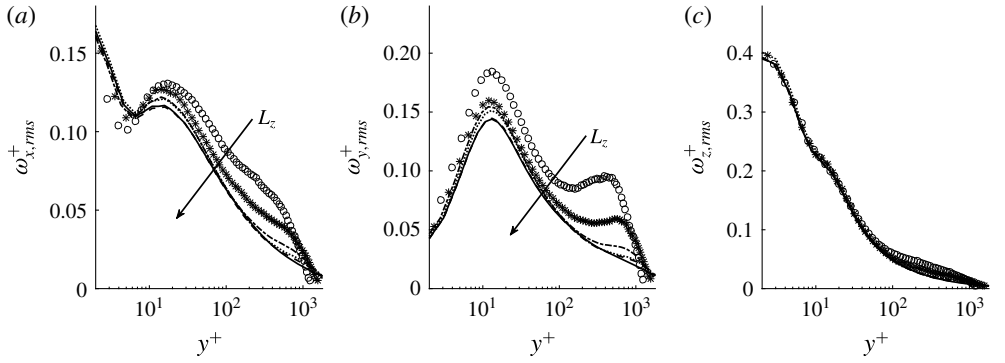

FIGURE 10. Vorticity fluctuations for different L_z with the box-confinement approach ($\lambda_{z,t} = L_z$): (*a*) $\omega^+_{x,rms}$; (*b*) $\omega^+_{y,rms}$; (*c*) $\omega^+_{z,rms}$. Here, ——, $L_z = 1.5h$; − − − −, $L_z = 1h$; · · · · · ·, $L_z = 0.75h$; − · − · −, $L_z = 0.5h$; ∗ $L_z = 0.3h$; ○ $L_z = 0.2h$.

velocity and the spanwise velocity spectra show non-negligibly large distortions even at $\lambda_z^+ \simeq 100$–200 (figure 9*b*,*c*). This indicates that the scale interaction is not localized only near the cutoff wavelength, $\lambda_z \simeq \lambda_{z,t}$.

The generation of such a 'tall' turbulent fluctuation both in the simulations with the box confinement and the artificial damping is reminiscent of the feature commonly observed in the minimal channel simulations using a small spanwise domain (e.g. Jiménez & Pinelli 1999; Hwang 2013, 2015). In the minimal channel, such a fluctuation has been understood to be induced by the remaining self-sustaining motions, as its removal does not significantly affect the statistics and dynamics of the remaining motions. Here, the appearance of such a fluctuation also with the artificial damping suggests that this is not a specific behaviour observed only in the confined spanwise domain, but may be an important general physical feature associated with a scale interaction occurring in the remaining motions. The spectra show that this fluctuation is responsible for generation of a considerable amount of Reynolds shear stress over a range of spanwise wavelength (figure 9*d*), explaining why the skin friction obtained by the box-confinement approach and the artificial damping is elevated than what is expected by the FIK identity.

Although the generation mechanism of the tall fluctuation is not entirely clear at the moment, a dimensional analysis, similar to the one given by Jiménez & Pinelli (1999), provides a physical insight into a possible origin of this behaviour. In a full domain simulation, the production in the logarithmic region would be $\mathcal{P} \sim u_\tau^3/y$, while dissipation is $\mathcal{E} \sim \nu\boldsymbol{\omega}^2$ where $\boldsymbol{\omega}$ is denoted as the total vorticity fluctuation. If the production and the dissipation are assumed to be locally balanced at each wall-normal location, this yields $\boldsymbol{\omega} \sim 1/y^{1/2}$, indicating that the vorticity fluctuation would decay with y. However, in the simulations with a narrow spanwise domain width L_z where the motions at $\lambda_z > L_z$ are not resolved, the production of the largest energy-containing motions resolved would be $\mathcal{P} \sim u_\tau^3/L_z$ due to $\lambda_z \sim y$. Therefore, the resulting $\boldsymbol{\omega}$ would become $\omega \sim 1/L_z^{1/2}$, indicating that the vorticity fluctuation in a confined spanwise domain would not significantly decay along the wall-normal direction, at least to some extent. Furthermore, the dimensional analysis indicates that the vorticity fluctuation would 'increase' as L_z is decreased.

Figure 10 reports the vorticity fluctuations for several L_z in the box-confinement approach (i.e. $\lambda_{z,t} = L_z$). Despite the fact that the present numerical experiments

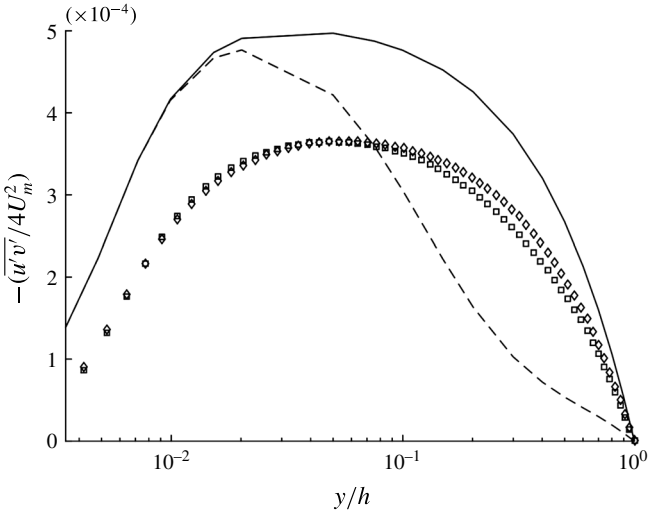

FIGURE 11. Comparison of the Reynolds shear stress: ——, DNS (Hoyas & Jiménez 2006); – – – –, FIK-identity-based approach; ◇, box-confinement approach; □, artificial damping of $F2000$. Here, the cutoff spanwise wavelength applied is $\lambda_{z,t} = 0.5h$.

are based on a set of large-eddy simulations, all the vorticity fluctuations indeed appear to increase on decreasing L_z, consistent with the dimensional analysis above. This behaviour is particularly prominent in the wall-normal vorticity statistics, and the wall-normal distribution also appears to be roughly constant for $10^2 < y^+ < 10^3$. This observation indicates that the dimensional analysis provides at least a partial explanation for the origin of the tall fluctuation. Given the dimensional analysis simply relying on the balance between production and dissipation, it is also important to mention that the mechanism of generation of the tall fluctuation would be associated with the energy cascade rather than the energy extraction of the large eddies from mean shear. In this respect, it is worth mentioning the recent work by Cimarelli *et al.* (2016), who showed the presence of the wall-normal energy flux progressing from smaller to larger attached eddies located further from the wall. This process might be related to the generation of the tall fluctuation, although other possible origins of the tall fluctuation should not be excluded.

Finally, it should be pointed out that all the spectra in figure 9 exhibit fairly good inner scaling for $y^+ < 100$–200 and $\lambda_z^+ < 100$–200. However, this does not necessarily mean that the original near-wall motions in the full simulation are not affected by the removal of the motions at $\lambda_z \simeq \lambda_{z,t}$. It should be stressed that the removal of large-scale motions either by the box-confinement approach or by the artificial damping reduces the skin friction, resulting in a reduced friction velocity. In other words, the good inner scaling nature of the spectra near $\lambda_z^+ \simeq 100$ in all the three simulations precisely implies that the removal of the motions at $\lambda_z \simeq \lambda_{z,t}$ makes the near-wall motions resettled such that they scale well with the 'new' inner units given by the reduced friction velocity.

The scale interaction process discussed above is also directly supported by the Reynolds shear stress distribution, as shown in figure 11. Here, we note that both of the box-confinement approach and the artificial damping are designed not to change the FIK identity itself. Therefore, the Reynolds shear stress profiles, normalized

by $2U_m$, are supposed to be directly related to their contribution to turbulent skin friction through the FIK identity in (2.4). Not surprisingly, all the Reynolds shear stress profiles obtained by applying the three approaches are overall smaller than that of full DNS. The profile obtained with the FIK-identity-based approach is almost identical to that of full DNS for $y/h \lesssim 0.01$, but is very different from those with the box-confinement approach and the artificial damping. In the region close to the wall ($y/h \lesssim 0.06$), the application of the FIK-identity-based approach to the full DNS data yield larger Reynolds shear stress than those with the other two approaches. This suggests that removing the motions larger than a given length scale indeed affects the near-wall motions such that they are adjusted to the reduced friction velocity. On the other hand, in the region relatively further from the wall ($y/h \gtrsim 0.06$), both of the box-confinement approach and the artificial damping exhibit larger Reynolds shear stress than that obtained with the FIK-identity-based approach. This indicates that the remaining motions in the absence of the motions at $\lambda_z > \lambda_{z,t}$ indeed generate additional Reynolds shear stress in this region, resulting in an elevated skin friction compared to what is expected from the FIK identity.

4.3. *Implications for flow control*

It has been consistently reported that the effectiveness of flow control strategies targeting the near-wall structures, such as opposition control (Chang *et al.* 2002) and spanwise wall oscillations (Quadrio 2011; Agostini *et al.* 2014), is reduced on increasing the Reynolds number. It has often been speculated that the undesirable performance degradation with the Reynolds number would possibly be due to the energetic large-scale structures such as large-scale and very-large scale motions (Touber & Leschziner 2012). However, the present finding suggests that this behaviour is rather due to a large number of self-similar energy-containing structures in the form of Townsend's attached eddies, most of which populate in the logarithmic region. In this respect, the trends shown by Hwang (2013) have been successfully extended to much higher Reynolds numbers (figure 5*b*).

It is also important to remember that the inhibition of the largest structures at scales $\lambda_z \geqslant 1.5h$ (i.e. VLSMs and LSMs) does not yield sufficiently large amounts of drag reduction, possibly due to the scale interaction discussed, even though they are expected to be responsible for 25–30 % of total skin friction at $Re_\tau = 2000$ according to the FIK-identity-based approach (figure 4): the removal of the motions at $\lambda_z \geqslant 0.75h$ by both of the box-confinement and the artificial damping approaches have reduced only 7–8 % of total skin friction. These levels of performance are a little discouraging, especially given the fact that the spanwise grooved surface (riblet), which does not require any external energy input to the system, has been shown to potentially give similar amounts of drag reduction, at least in optimal conditions (Walsh 1982; Squire & Savill 1989; Choi, Moin & Kim 1993; Viswanath 2002; Spalart & McLean 2011). It is also worth noting that the amount of skin-friction reduction with the removal of the largest structures does not appear to be highly dependent upon the way of removing and/or disturbing these motions. For example, destruction of the self-sustaining process of these motions through inhibition of the lift-up effect also yielded 8 % of skin-friction reduction at $Re_\tau \simeq 950$ (Hwang & Bengana 2016), a value not very different from that obtained here. Of course, it is still too early to conclude that this value would be the largest amount of drag reduction possible by inhibiting the largest structures.

Despite this discouraging postulation, it is still hopeful to observe the outer scaling behaviour of the normalized skin friction with gradual removal of the motions from

the largest scale (see figure 6). This observation suggests that a drag reduction of 20–30 % may be achievable with an array of actuators and/or sensors, the size of which is only an order of magnitude smaller than the outer length scale. Since the boundary-layer thickness over wing or surface of a commercial aircraft is $O(1\ \text{cm})$ (Kasagi, Suzuki & Fukagata 2009), the expected size of the actuators and sensors would be $O(1\ \text{mm})$, significantly relieving the micro-scale design restriction posed by targeting the near-wall structures (Kasagi *et al.* 2009).

5. Concluding remarks

Thus far, we have assessed the contribution of the energy-containing motions in the form of Townsend's attached eddies to turbulent skin friction at sufficiently high Reynolds numbers. In particular, skin-friction generation by the motions, the spanwise size of which is smaller than a given cutoff wavelength (i.e. $\lambda_z \leqslant \lambda_{z,t}$), has been quantified by employing three different approaches: (i) the FIK-identity-based approach; (ii) the box-confinement approach; (iii) artificial damping. The near-wall motions have been found to continuously lose their importance on increasing the Reynolds number, consistent with the previous finding at low Reynolds numbers (Hwang 2013). However, interestingly, the largest structures (i.e. very-large-scale and large-scale motions) at $\lambda_z = 1.5h$ have also been found to be of limited importance: although the FIK-identity-based approach shows that the largest motions at $\lambda_z = 1.5h$ (i.e. large-scale and very-large-scale motions) are responsible for 20–30 % of total skin friction at $Re_\tau \simeq 2000$, their actual removal by the box-confinement and the artificial damping approaches yields only 5–8 % of skin-friction reduction, possibly due to a non-trivial scale interaction. All the three methods have consistently revealed that the largest amount of skin friction is generated by the self-similar energy-containing motions, the spanwise size of which lie between $\lambda_z^+ \simeq 100$ and $\lambda_z \simeq 1.5h$ at sufficiently high Reynolds numbers. These motions essentially belong to the logarithmic region in the sense that their size is proportional to the distance from the wall (Hwang 2015), and their contribution has been found to gradually increase with the value of Re_τ, eventually being responsible for most of turbulent skin-friction generation. The significance of attached eddies to drag is also shown by the probability density function of wall-shear stress, which retains its fundamental characteristics of positive skewness even with the removal of the largest eddies. Finally, it has been shown that the normalized skin-friction reduction with respect to the cutoff spanwise wavelength $\lambda_{z,t}$ scales in the outer unit (figure 6), at least in the range of Reynolds number investigated in the present study.

The next step of the present study would be naturally to control the self-similar energy-containing motions for an appreciable amount of drag reduction. However, the multi-scale skin-friction generation involving little understood scale interactions suggests that designing a practically realizable flow controller would be highly challenging. Simple trial and error approaches would be unlikely to work for this problem, and much more innovative and systematic approaches need to be taken with very careful inspection of the given system.

Acknowledgements

Y.H. was supported by the Engineering and Physical Sciences Research Council (EPSRC) in the UK (EP/N019342/1). H.C. was supported by the NRF program (No. NRF-2014M3C1B1033848) of MSIP, Korea.

Case	Re_m	Re_τ	L_x/h	L_z/h	Δx^+	Δz^+	Δy_1^+	C_f $(\times 10^{-3})$	$\Delta C_f(\%)$
*M*2000*a*	89 100	1863	1.0	0.5	58.2	29.1	1.31	3.50	1.7
*L*2000*a*	89 100	1854	2.0	0.5	57.9	28.9	1.30	3.46	0.6
*VL*2000*a*	89 100	1848	4.0	0.5	57.7	28.8	1.30	3.44	Ref.
*M*2000	89 100	2070	3.0	1.5	64.7	32.3	1.45	4.32	1.4
*L*2000	89 100	2061	6.0	1.5	64.4	32.2	1.44	4.28	0.5
*VL*2000	89 100	2056	9.0	1.5	64.2	32.1	1.44	4.27	Ref.

TABLE 3. Effect of the streamwise computational domain on the friction coefficient with $L_z = 0.5h$ and $L_z = 1.5h$. Here, $\Delta C_f = |C_f - C_{f,0}|/C_{f,0}$ where $C_{f,0}$ is the friction coefficient of each of the reference cases (i.e. *VL*2000*a* for $L_z = 0.5h$ and *VL*2000 for $L_z = 1.5h$). Note that, for each L_z, the case with the longest streamwise domain is chosen as the reference case.

Appendix A. Comparison of box streamwise domain

The effect of the streamwise domain size on the skin-friction coefficient is examined here for $L_z = 0.5h$ and $L_z = 1.5h$, and is reported in table 3. For $L_z = 1.5h$, three different streamwise domains are tested with $L_x = 3, 6, 9h$. The skin friction changes little with $\Delta C_f < 2\,\%$ even for $L_x = 2L_z$, as one would have expected from the existing literature (e.g. Lozano-Durán & Jiménez 2014). In the case of $L_z = 0.5h$, this behaviour remains essentially the same, justifying the use of a short streamwise domains for the box-confinement approach.

Appendix B. Influence of uniform spanwise mode on small and large streamwise computational domains

With the box-confinement approach applied to DNS at low Reynolds numbers, it was previously shown that the role of the spanwise uniform mode ($k_z = 0$) in turbulent skin friction is very limited (Hwang 2013). Here, the related discussion is further extended for larger $L_z(= \lambda_{z,t})$, and, in particular, here we show that the effect of the uniform spanwise mode in a short streamwise computational domain is even smaller than that in a long streamwise computational domain. This is presumably because the short streamwise computational domain does not allow for the streamwise space required for the spanwise uniform motion, which was found to be energetic at $\lambda_x \simeq 2$–$4h$ (Hwang 2013). Figure 12 shows the spanwise wavenumber spectra of following three tested cases for $L_z = 0.5h$: (i) the short domain ($L_x = 1.0h$) with the spanwise uniform mode (solid; *M*2000*a* in table 3); (ii) the short domain ($L_x = 1.0h$) without the spanwise uniform mode (dashed); (iii) the long domain at least for this case ($L_x = 4h$) without the spanwise uniform mode (shaded). Overall, the spectra of the three tested cases do not show significant differences from one another, except for the streamwise velocity spectra. However, this may have been expected, given the streamwise elongated nature of the streamwise velocity fluctuation. The overall deviation of the spectra (especially for the Reynolds shear stress) appear to be reasonably small, suggesting the relatively minor roles of the spanwise uniform mode and the streamwise box size. The role of the spanwise uniform mode in the first- and second-order statistics is also examined for $L_z = 0.5h$, as reported in figure 13. The change in the mean velocity appears to be small, consistent with the very

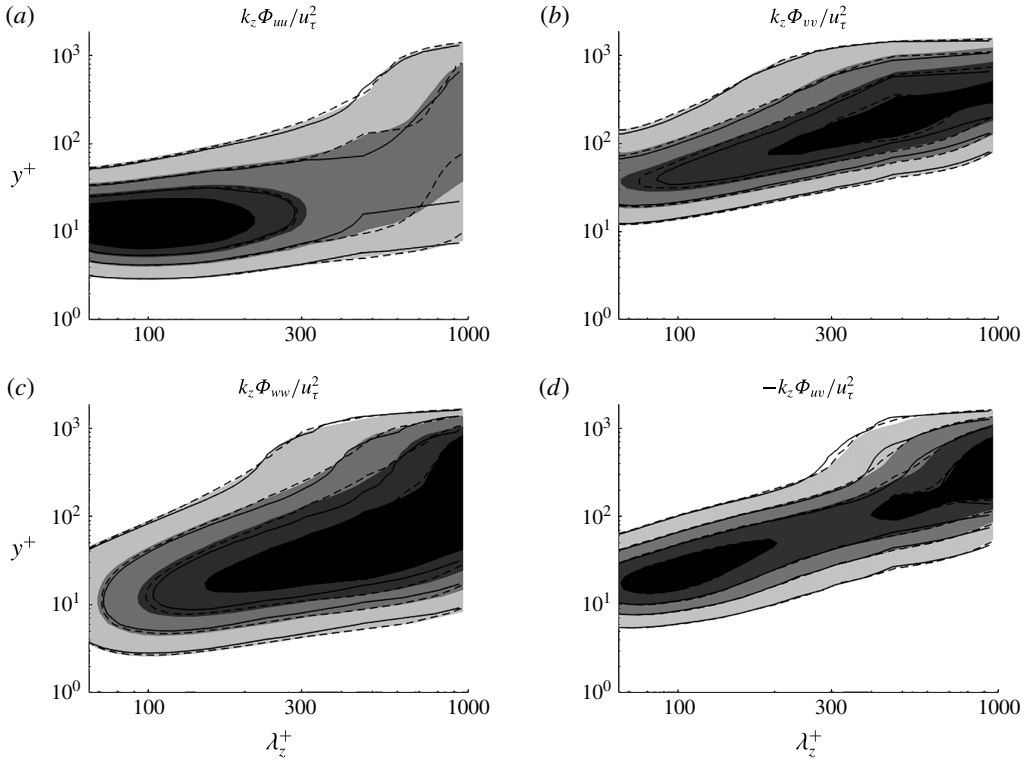

FIGURE 12. Premultiplied one-dimensional spanwise wavenumber spectra of (*a*) streamwise, (*b*) wall-normal, (*c*) spanwise velocities and (*d*) Reynolds shear stress for $L_z = 0.5h$. Here, the solid, dashed and shaded contours indicate $L_x = 1h$ with the spanwise uniform mode (*M*2000*a*), $L_x = 1h$ without the spanwise uniform mode and $L_x = 4h$ without the spanwise uniform mode, respectively. The contour labels are chosen to be 0.2, 0.4, 0.6, 0.8 times each of the maximum for comparison.

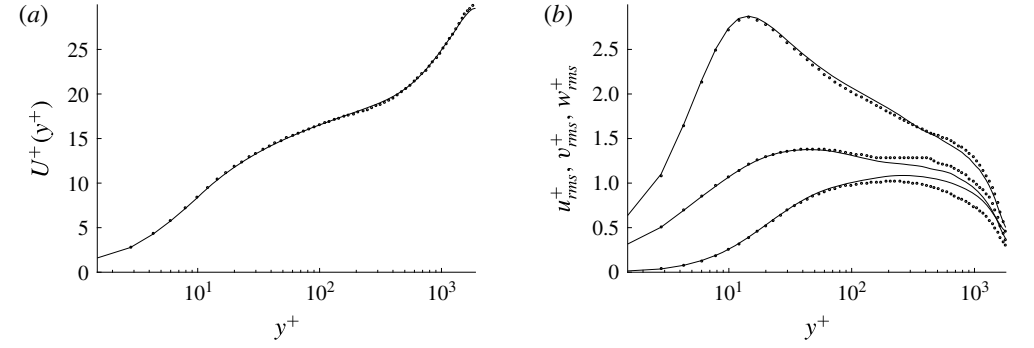

FIGURE 13. (*a*) Mean-velocity profile and (*b*) turbulent velocity fluctuations at $Re_\tau \approx 2000$ ($L_x = 1h$): ——, $L_z = 0.5h$ with uniform mode; ○, $L_z = 0.5h$ without uniform mode.

small change in C_f in figure 4. Non-negligible effects were observed in the velocity fluctuations, but these also appear to be small and insignificant, explaining the minor role of the spanwise uniform mode in skin-friction generation.

REFERENCES

ABE, H., KAWAMURA, H. & CHOI, H. 2004 Very large-scale structures and their effects on the wall shear-stress fluctuations in a turbulent channel flow up to $Re_\tau = 640$. *Trans. ASME J. Fluids Engng* **126** (5), 835.

AGOSTINI, L. & LESCHZINER, M. 2016 Predicting the response of small-scale near-wall turbulence to large-scale outer motions. *Phys. Fluids* **28** (1), 015107.

AGOSTINI, L., TOUBER, E. & LESCHZINER, M. A. 2014 Spanwise oscillatory wall motion in channel flow: drag-reduction mechanisms inferred from DNS-predicted phase-wise property variations at $Re_\tau = 1000$. *J. Fluid Mech.* **743**, 606–635.

DEL ALAMO, J. C. & JIMÉNEZ, J. 2003 Spectra of the very large anisotropic scales in turbulent channels. *Phys. Fluids* **15** (6), 41–44.

DEL ALAMO, J. C., JIMÉNEZ, J., ZANDONADE, P. & MOSER, R. D. 2004 Scaling of the energy spectra of turbulent channels. *J. Fluid Mech.* **500**, 135–144.

DEL ALAMO, J. C., JIMÉNEZ, J., ZANDONADE, P. & MOSER, R. D. 2006 Self-similar vortex clusters in the turbulent logarithmic region. *J. Fluid Mech.* **561**, 329–358.

BAARS, W. J., TALLURU, K. M., HUTCHINS, N. & MARUSIC, I. 2015 Wavelet analysis of wall turbulence to study large-scale modulation of small scales. *Exp. Fluids* **56** (10), 1–15.

BENGANA, Y. & HWANG, Y. 2015 Minimal dynamics of self-sustaining attached eddies in a turbulent channel. In *International Symposium on Turbulent Shear Flow, Melbourne,* 4A-2.

BERNARDINI, M., PIROZZOLI, S. & ORLANDI, P. 2014 Velocity statistics in turbulent channel flow up to $Re_\tau = 4000$. *J. Fluid Mech.* **742**, 171–191.

BLESBOIS, O., CHERNYSHENKO, S. I., TOUBER, E. & LESCHZINER, M. A. 2013 Pattern prediction by linear analysis of turbulent flow with drag reduction by wall oscillation. *J. Fluid Mech.* **724**, 607–641.

BUSHNELL, D. M. 2002 Aircraft drag reduction – a review. *J. Aerosp. Engng* **217**, 1–18.

CHANG, Y., COLLIS, S. S. & RAMAKRISHNAN, S. 2002 Viscous effects in control of near-wall turbulence. *Phys. Fluids* **14** (11), 4069–4080.

CHERNYSHENKO, S. I. & BAIG, M. F. 2005 The mechanism of streak formation in near-wall turbulence. *J. Fluid Mech.* **544**, 99–131.

CHERNYSHENKO, S. I., MARUSIC, I. & MATHIS, R. 2012 Quasi-steady description of modulation effects in wall turbulence. arXiv:1203.3714v1 [physics.flu-dyn], p. 16.

CHOI, H., MOIN, P. & KIM, J. 1993 Direct numerical simulation of turbulent flow over riblets. *J. Fluid Mech.* **255**, 503–539.

CHOI, H., MOIN, P. & KIM, J. 1994 Active turbulence control for drag reduction in wall-bounded flows. *J. Fluid Mech.* **262**, 75–110.

CIMARELLI, A., DE ANGELIS, E., JIMÉNEZ, J. & CASCIOLA, C. M. 2016 Cascades and wall-normal fluxes in turbulent channel flows. *J. Fluid Mech.* **796**, 417–436.

COSSU, C., PUJALS, G. & DEPARDON, S. 2009 Optimal transient growth and very large scale structures in turbulent boundary layers. *J. Fluid Mech.* **619**, 79–94.

DEAN, R. B. 1978 Reynolds number dependence of skin friction and other bulk flow variables in two-dimensional rectangular duct flow. *Trans. ASME J. Fluids Engng* **100**, 215–223.

DECK, S., RENARD, N., LARAUFIE, R. & WEISS, P.-É. 2014 Large-scale contribution to mean wall shear stress in high-Reynolds-number flat-plate boundary layers up to $Re_\theta = 13\,650$. *J. Fluid Mech.* **743**, 202–248.

DUKOWICZ, J. K. & DVINSKY, A. S. 1992 Approximate factorization as a high order splitting for the implicit incompressible flow equations. *J. Comput. Phys.* **102** (2), 336–347.

FLORES, O. & JIMÉNEZ, J. 2010 Hierarchy of minimal flow units in the logarithmic layer. *Phys. Fluids* **22** (7), 1–4.

FUKAGATA, K., IWAMOTO, K. & KASAGI, N. 2002 Contribution of Reynolds stress distribution to the skin friction in wall-bounded flows. *Phys. Fluids* **14** (11), 13–17.

GARCÍA-MAYORAL, R. & JIMÉNEZ, J. 2011 Drag reduction by riblets. *Phil. Trans. R. Soc. Lond.* A **369** (1940), 1412–1427.

GATTI, D. & QUADRIO, M. 2013 Performance losses of drag-reducing spanwise forcing at moderate values of the Reynolds number. *Phys. Fluids* **25** (12), 125109.

GERMANO, M., PIOMELLI, U., MOIN, P. & CABOT, W. H. 1991 A dynamic subgrid-scale eddy viscosity model. *Phys. Fluids* A **3**, 1760–1765.

GULLBRAND, J. 2000 An evaluation of a conservative fourth order DNS code in turbulent channel flow. In *Cent. Turbul. Res. Annu. Briefs*, pp. 211–218.

HAMILTON, J. M., KIM, J. & WALEFFE, F. 1995 Regeneration mechanisms of near-wall turbulence structures. *J. Fluid Mech.* **287**, 317–348.

HOYAS, S. & JIMÉNEZ, J. 2006 Scaling of the velocity fluctuations in turbulent channels up to $Re_\tau = 2003$. *Phys. Fluids* **18** (1), 1–4.

HUTCHINS, N. & MARUSIC, I. 2007*a* Evidence of very long meandering features in the logarithmic region of turbulent boundary layers. *J. Fluid Mech.* **579**, 1–28.

HUTCHINS, N. & MARUSIC, I. 2007*b* Large-scale influences in near-wall turbulence. *Phil. Trans. R. Soc. Lond.* A **365** (1852), 647–664.

HWANG, Y. 2013 Near-wall turbulent fluctuations in the absence of wide outer motions. *J. Fluid Mech.* **723**, 264–288.

HWANG, Y. 2015 Statistical structure of self-sustaining attached eddies in turbulent channel flow. *J. Fluid Mech.* **767**, 254–289.

HWANG, Y. & BENGANA, Y. 2016 Self-sustaining process of minimal attached eddies in turbulent channel flow. *J. Fluid Mech.* **795**, 708–738.

HWANG, Y. & COSSU, C. 2010*a* Linear non-normal energy amplification of harmonic and stochastic forcing in the turbulent channel flow. *J. Fluid Mech.* **664**, 51–73.

HWANG, Y. & COSSU, C. 2010*b* Self-sustained process at large scales in turbulent channel flow. *Phys. Rev. Lett.* **105** (4), 1–10.

HWANG, Y. & COSSU, C. 2011 Self-sustained processes in the logarithmic layer of turbulent channel flows. *Phys. Fluids* **23** (6), 061702.

JEONG, J. & HUSSAIN, F. 1997 Coherent structures near the wall in a turbulent channel flow. *J. Fluid Mech.* **332**, 185–214.

JIMÉNEZ, J. & HOYAS, S. 2008 Turbulent fluctuations above the buffer layer of wall-bounded flows. *J. Fluid Mech.* **611**, 215–236.

JIMÉNEZ, J. & MOIN, P. 1991 The minimal flow unit in near-wall turbulence. *J. Fluid Mech.* **225**, 231–240.

JIMÉNEZ, J. & PINELLI, A. 1999 The autonomous cycle of near-wall turbulence. *J. Fluid Mech.* **389**, 335–359.

JUNG, W., MANGIAVACCHI, N. & AKHAVAN, R. 1992 Suppression of turbulence in wall-bounded flows by high-frequency spanwise oscillations. *Phys. Fluids* **4** (8), 1605–1607.

KASAGI, N., SUZUKI, Y. & FUKAGATA, K. 2009 Microelectromechanical systems-based feedback control of turbulence for skin friction reduction. *Annu. Rev. Fluid Mech.* **41** (1), 231–251.

KEIRSBULCK, L., LABRAGA, L. & GAD-EL-HAK, M. 2012 Statistical properties of wall shear stress fluctuations in turbulent channel flows. *Intl J. Heat Fluid Flow* **37**, 1–8.

KIM, J. & LIM, J. 2000 A linear process in wall-bounded turbulent shear flows. *Phys. Fluids* **12** (8), 1885–1888.

KIM, J., MOIN, P. & MOSER, R. D. 1987 Turbulence statistics in fully developed channel flow at low Reynolds number. *J. Fluid Mech.* **177**, 133–166.

KIM, K. C. & ADRIAN, R. J. 1999 Very large-scale motion in the outer layer. *Phys. Fluids* **11** (2), 417–422.

KLINE, S. J., REYNOLDS, W. C., SCHRAUB, F. A. & RUNDSTATLER, P. W. 1967 The structure of turbulent boundary layers. *J. Fluid Mech.* **30**, 741–773.

KORNILOV, V. I. 2015 Current state and prospects of researches on the control of turbulent boundary layer by air blowing. *Prog. Aerosp. Sci.* **76**, 1–23.

KOVASZNAY, L. S. G. 1970 The turbulent boundary layer. *Annu. Rev. Fluid Mech.* **2** (1), 95–112.

KRAVCHENKO, A. G., CHOI, H. & MOIN, P. 1993 On the relation of near-wall streamwise vortices to wall skin friction in turbulent boundary layers. *Phys. Fluids* A **5** (12), 3307–3309.

KRAVCHENKO, A. G. & MOIN, P. 1997 On the effect of numerical errors in large eddy simulations of turbulent flows. *J. Comput. Phys.* **131**, 310–322.

LANDAHL, M. T. 1990 On sublayer streaks. *J. Fluid Mech.* **212**, 593–614.

LEE, M. & MOSER, R. D. 2015 Direct numerical simulation of turbulent channel flow up to $Re_\tau = 5200$. *J. Fluid Mech.* **774**, 395–415.

LIM, J. & KIM, J. 2004 A singular value analysis of boundary layer control. *Phys. Fluids* **16** (6), 1980–1988.

LOZANO-DURÁN, A. & JIMÉNEZ, J. 2014 Time-resolved evolution of coherent structures in turbulent channels: characterization of eddies and cascades. *J. Fluid Mech.* **759**, 432–471.

LUHAR, M., SHARMA, A. S. & MCKEON, B. J. 2014 On the structure and origin of pressure fluctuations in wall turbulence: predictions based on the resolvent analysis. *J. Fluid Mech.* **751**, 38–70.

MARUSIC, I. & KUNKEL, G. J. 2003 Streamwise turbulence intensity formulation for flat-plate boundary layers. *Phys. Fluids* **15** (8), 2461–2464.

MARUSIC, I., MATHIS, R. & HUTCHINS, N. 2010 High Reynolds number effects in wall turbulence. *Intl J. Heat Fluid Flow* **31** (3), 418–428.

MARUSIC, I., MONTY, J. P., HULTMARK, M. & SMITS, A. J. 2013 On the logarithmic region in wall turbulence. *J. Fluid Mech.* **716**, R3.

MATHIS, R., HUTCHINS, N. & MARUSIC, I. 2009 Large-scale amplitude modulation of the small-scale structures in turbulent boundary layers. *J. Fluid Mech.* **628**, 311–337.

MATHIS, R., MARUSIC, I., CHERNYSHENKO, S. I. & HUTCHINS, N. 2013 Estimating wall-shear-stress fluctuations given an outer region input. *J. Fluid Mech.* **715**, 163–180.

MOARREF, R. & JOVANOVIĆ, M. R. 2012 Model-based design of transverse wall oscillations for turbulent drag reduction. *J. Fluid Mech.* **707**, 205–240.

ORLANDI, P. & JIMENEZ, J. 1994 On the generation of turbulent wall friction. *Phys. Fluids* **6** (2), 634.

PARK, J., HWANG, Y. & COSSU, C. 2011 On the stability of large-scale streaks in turbulent Couette and Poiseulle flows. *C. R. Mec.* **339** (1), 1–5.

PARK, N., LEE, S., LEE, J. & CHOI, H. 2006 A dynamic subgrid-scale eddy viscosity model with a global model coefficient. *Phys. Fluids* **18**, 125109.

PERRY, A. E. & CHONG, M. S. 1982 On the mechanism of wall turbulence. *J. Fluid Mech.* **119**, 173–217.

PUJALS, G., GARCÍA-VILLALBA, M., COSSU, C. & DEPARDON, S. 2009 A note on optimal transient growth in turbulent channel flows. *Phys. Fluids* **21** (1), 1–6.

QUADRIO, M. 2011 Drag reduction in turbulent boundary layers by in-plane wall motion. *Phil. Trans. R. Soc. Lond.* A **369** (1940), 1428–1442.

RENARD, N. & DECK, S. 2016 A theoretical decomposition of mean skin friction generation into physical phenomena across the boundary layer. *J. Fluid Mech.* **790**, 339–367.

SARGHINI, F., PIOMELLI, U. & BALARAS, E. 1999 Scale-similar models for large-eddy simulations. *Phys. Fluids* **11** (6), 1596–1607.

SCHLATTER, P., ÖRLÜ, R., LI, Q., BRETHOUWER, G., FRANSSON, J. H. M., JOHANSSON, A. V., ALFREDSSON, P. H. & HENNINGSON, D. S. 2009 Turbulent boundary layers up to $Re_\theta = 2500$ studied through simulation and experiment. *Phys. Fluids* **21** (5), 051702.

SCHOPPA, W. & HUSSAIN, F. 2002 Coherent structure generation in near-wall turbulence. *J. Fluid Mech.* **453**, 57–108.

SCHULTZ, M. P. & FLACK, K. A. 2013 Reynolds-number scaling of turbulent channel flow. *Phys. Fluids* **25** (2), 1–13.

DE SILVA, C. M., GNANAMANICKAM, E. P., ATKINSON, C., BUCHMANN, N. A., HUTCHINS, N., SORIA, J. & MARUSIC, I. 2014 High spatial range velocity measurements in a high Reynolds number turbulent boundary layer. *Phys. Fluids* **26** (2), 025117.

SPALART, P. R. & MCLEAN, J. D. 2011 Drag reduction: enticing turbulence, and then an industry. *Phil. Trans. R. Soc. Lond.* A **369** (1940), 1556–1569.

SQUIRE, L. C. & SAVILL, A. M. 1989 Drag measurements on planar riblet surfaces at high subsonic speeds. *Appl. Sci. Res.* **46** (3), 229–243.

STADSTED, O. & MOIN, P. 1991 On the mechanics of 3-D turbulent boundary layer. In *Proc. Eighth Symp. Turbul. Shear Flows, Munich*.

TOMKINS, C. D. & ADRIAN, R. J. 2003 Spanwise structure and scale growth in turbulent boundary layers. *J. Fluid Mech.* **490**, 37–74.

TOMKINS, C. D. & ADRIAN, R. J. 2005 Energetic spanwise modes in the logarithmic layer of a turbulent boundary layer. *J. Fluid Mech.* **545**, 141.

TOUBER, E. & LESCHZINER, M. A. 2012 Near-wall streak modification by spanwise oscillatory wall motion and drag-reduction mechanisms. *J. Fluid Mech.* **693**, 150–200.

TOWNSEND, A. A. 1961 Equilibrium layers and wall turbulence. *J. Fluid Mech.* **12**, 97–120.

TOWNSEND, A. A. 1976 *The Structure of Turbulent Shear Flow*, 1st edn. Cambridge University Press.

VISWANATH, P. R. 2002 Aircraft viscous drag reduction using riblets. *Prog. Aerosp. Sci.* **38** (6–7), 571–600.

VREMAN, A. W. 2004 An eddy-viscosity subgrid-scale model for turbulent shear flow: algebraic theory and applications. *Phys. Fluids* **16** (10), 3670–3681.

WALSH, M. J. (Ed.) 1982 *Turbulent Boundary Layer Drag Reduction using Riblets, 20th AIAA Aerospace Sciences Meeting, Orlando, FL.*

ZANOUN, E.-S., NAGIB, H. & DURST, F. 2009 Refined c_f relation for turbulent channels and consequences for high-*Re* experiments. *Fluid Dyn. Res.* **41** (2), 021405.